AGU100 ADVANCING EARTH AND SPACE SCIENCE

JGR Solid Earth

RESEARCH ARTICLE
10.1029/2019JB018416

**Key Points:**
- We present a beamforming method to extract the phase velocity of the Rayleigh wave directly from the ambient noise, without interferometry
- A 3D *Vs* model of NE Tibet is established by inverting the obtained Rayleigh wave velocity maps
- Mid crustal low velocity zones are observed in the Songpan-Ganzi Terrane and in NW Qilian Orogen

**Supporting Information:**
- Supporting Information S1

**Correspondence to:**
L. Lu,
laiyulu@cea-igp.ac.cn

**Citation:**
Wang, K., Lu, L., Maupin, V., Ding, Z., Zheng, C., & Zhong, S. (2020). Surface wave tomography of northeastern tibetan plateau using beamforming of seismic noise at a dense array. *Journal of Geophysical Research: Solid Earth*, *125*, e2019JB018416. https://doi.org/10.1029/2019JB018416

Received 23 JUL 2019
Accepted 22 MAR 2020
Accepted article online 27 MAR 2020



# Surface Wave Tomography of Northeastern Tibetan Plateau Using Beamforming of Seismic Noise at a Dense Array

**Kaiming Wang[1], Laiyu Lu[1], Valérie Maupin[2], Zhifeng Ding[1], Chen Zheng[1], and Shijun Zhong[3]**

[1]Institute of Geophysics, China Earthquake Administration, Beijing, China, [2]CEED, Department of Geosciences, University of Oslo, Oslo, Norway, [3]Beijing Earthquake Agency, Beijing, China

**Abstract** In traditional surface wave tomography based on seismic noise, 2D phase or group velocity distribution is obtained by performing pure-path inversion after extracting interstation velocities based on the noise cross-correlation function. In this paper, we show that 2D surface wave phase velocity maps of adequate quality can be obtained directly, without interferometry, by beamforming the ambient noise recorded at array of stations. This method does not require a good azimuthal distribution of the noise sources. The 2D surface wave phase velocity map is obtained by moving the subarrays within a larger dense network of stations. The method is illustrated with seismic noise recorded by over 600 stations of the ChinArray (Phase II). We obtain 2D Rayleigh wave phase velocity maps between 7 and 35 s in Northeastern (NE) Tibetan Plateau and adjacent regions that compare well with results obtained with other methods. The shear wave velocity model is then derived by inverting the phase velocity with depth. The model correlates well with geology and tectonics in NE Tibet. Two clear mid-to-low crustal low-velocity zones are observed at 15- to 35-km depth beneath the Songpan-Ganzi terrane and Northwestern Qilian Orogen, possibly facilitating lower crustal flow in this key region for the tectonic evolution of NE Tibet.

## 1. Introduction

Imaging of subsurface structures using surface waves recorded at seismological stations can be done in different ways. Tomographic inversion of earthquake observables like group times, phases, or waveforms recorded either globally or regionally has a long tradition (e.g., Montagner, 1986; Romanowicz, 2002; Woodhouse & Dziewonski, 1984). Interstation cross-correlated noise is also used routinely as data basis for surface wave tomography (e.g., Campillo et al., 2011; Sens-Schöenfelder & Wegler, 2011; Shapiro et al., 2005). It provides data in a frequency range particularly well suited for crustal studies and is also advantageous in terms of lateral resolution as it gives velocity measurements along interstation paths which are usually much shorter than earthquake-station paths. A major issue with this methodology is however that the extraction of proper Green's functions from interstation noise cross-correlation requires in theory noise sources well-distributed in azimuth. In practice, it must be noted though that the results, in particular those based on phase and phase velocities, are rather robust to uneven noise distribution and that correction stategies have be devised (Froment et al., 2010; Sadeghisorkhani et al., 2017; Tsai, 2009; Yao & van der Hilst, 2009).

An approach completely different from the tomographic one is the local tracking of the phase variation of a wavefront, also called eikonal tomography. Originally applied to earthquake data (Alsina et al., 1993; Friederich, 1998; Weidle, 2012), this approach has also been used more recently with the Green's functions obtained from noise cross-correlation (Lin et al., 2009; Ritzwoller et al., 2011; Tomar et al., 2017). This methodology has been boosted in recent years by the deployment of large and dense networks and can in theory provide models with high lateral resolution, up to the interstation distance. Amplitude variations within the network, which are diagnostic of deviation from the plane wave model, do however bias the measured phase velocity if only phase variations are considered (Friederich et al., 1998; Wielandt, 1993). This bias can be corrected for if the second-order lateral derivatives of the amplitudes can be evaluated, but this proves to be difficult to achieve in practice.

Beamforming provides an alternative to phase-tracking, improving robustness at the expense of resolution. It provides a measure of the correlation of the phase at an array of stations with the phase of a plane wave

(Rost & Thomas, 2002). For surface waves, the plane wave model can be replaced with cylindrical waves originating at the source to account for the expected curvature of the wavefront (Forsyth & Li, 2005; Maupin, 2011). The output is the apparent horizontal velocity and backazimuth of the plane or cylindrical wave (possibly of several interfering waves) that fits best the actual data. For surface waves, and in the absence of large deviations from the wave model, the apparent velocity is equal to the average local phase velocity at the location of the array (Friederich et al., 1998). Beamforming using different subsets of the stations of a larger network, also called subarrays, provides therefore the opportunity to directly map phase velocity variations across the network without a tomographic inversion. As the eikonal tomography, beamforming suffers from biases related to amplitude variations caused by deviation from incident plane wave structure or inhomogeneities within the network (Friederich et al., 1998), but this is less severe for large subarrays, and can be partly compensated by using waves incident from several directions (Bodin & Maupin, 2008).

Although most applications of surface wave beamforming have been done using earthquake data, raw ambient noise (raw meaning without interstation cross-correlation) can also be used and yield primarily information on Rayleigh wave propagation. Beamforming of noise was first used by Gerstoft and Tanimoto (2007) to determine the temporal variation of the noise sources backazimuth in California over 1 year, which they could obtain with a time resolution of 1.5 h. Behr et al. (2013) studied the source regions and noise generation mechanisms for both Rayleigh and Love waves in the Southern Hemisphere by beamforming three-component noise recordings at a dense array in New Zealand. The velocity obtained by noise beamforming was first exploited by Harmon et al. (2008) using data from the Tomography Under Costa Rica and Nicaragua project (TUCAN) array. The rather small dimension of the array did not allow them to use subarrays, but the velocity obtained using the whole array was used to validate the phase velocities obtained with the more common time-frequency analysis of cross-correlation functions. Their study suggests that two methods give the same results within 1% error.

A more recent study by Roux and Ben-Zion (2017) using subarrays of the Californian network proves the feasibility of using noise beamforming for mapping phase velocity lateral variations. As beamforming is based on correlating the phase of the data with a plane wave model, it does not require, as the noise cross-correlation function method, that interference of noise from different directions let the interstation Green's function emerge. It has therefore the great advantage that much shorter time series can be used, down to a few hours (Gerstoft & Tanimoto, 2007; Harmon et al., 2008; Roux & Ben-Zion, 2017), and is not affected by non-uniform azimuthal distribution of the noise sources, at least as long as azimuthal anisotropy is not an issue (Alvizuri & Tanimoto, 2011; Lu et al., 2018).

The frequency range of the noise provides information on Rayleigh wave phase velocities at higher frequency than teleseismic earthquake data and is usually better suited for crustal studies. In this paper, we use beamforming of noise to produce Rayleigh wave phase velocity maps for the Northeast Tibetan Plateau (NETP) and invert them with depth to construct a 3D shear wave velocity structure of the Plateau, with particular emphasis on the crustal structure. As one of the youngest part in the Tibetan Plateau, NETP has suffered severe deformation since the late Cenozoic and is still at an early stage of lithosphere deformation. As such, it is a key place to explore continental evolution and dynamics. Several continental dynamics models have been proposed to interpret the Tibetan Plateau deformation and crustal thickening. Molnar and Tapponnier (1975) presented a model where oblique subduction of Asian lithosphere and extrusion along left lateral strike-slip faults make crustal thickening viable (Tapponnier & Molnar, 1997). Through numerical modeling of a thin viscous sheet, England and Houseman (1986) showed that the entire lithosphere is thickened with shortening of crust and mantle. Clark and Royden (2000) and Royden et al. (2008) proposed a crustal channel flow model where mid-to-low crustal material below central Tibet flows and escapes to the margins of the Tibetan Plateau through several channels. This last model is consistent with the mid-crustal low-velocity layers observed in NETP by surface wave tomography based on earthquake data and ambient noise (e.g., Bao et al., 2013; Li et al., 2014a; Yang et al., 2012). However, due to the limitations and characteristics of the imaging methods, the location and intensity of these important mid-crustal low-velocity layers vary between these tomography studies, and we will therefore pay special attention to their resolution in our model.

The paper is organized as follows: we start with the elaboration of the method and data processing, introducing the beamforming method to extract the 2D phase maps of Rayleigh waves and analyzing its potential resolution. 2D phase maps and the reliability of the method is investigated in section 3 by comparison with the results generated by other methods. A 3D S-wave velocity model of NETP and tectonic implications are presented in section 4, followed by conclusions.

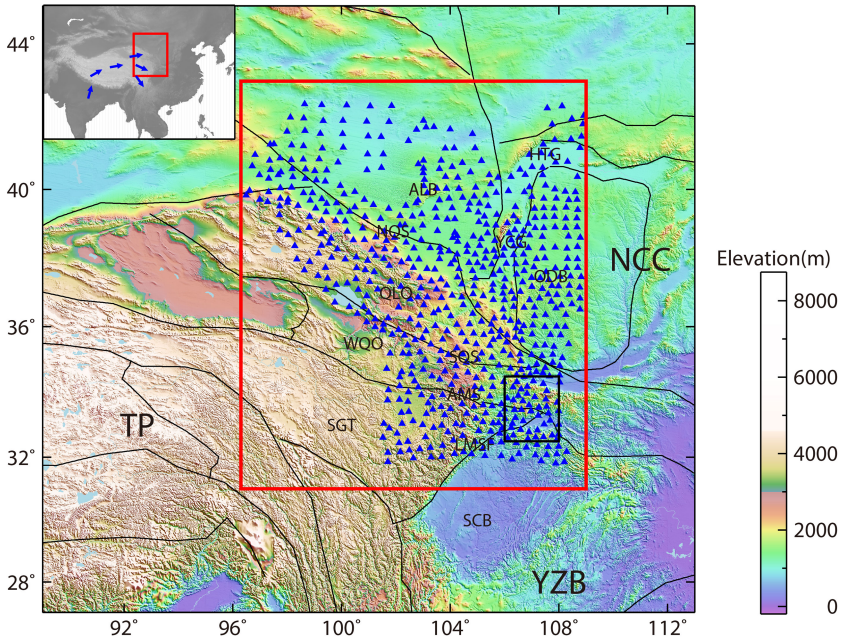


**Figure 1.** Tectonic features in the northeast margin of Tibetan Plateau and adjacent region. Black lines represent the boundaries of the main tectonic sutures. The red box is the research area. The stations in Chinarray Phase II are denoted by blue triangles. The subarray labeled by the black box is shown as an example for beamforming in Figure 2. The blue arrows indicate the large scale block motion (Liu et al., 2014). AMS = Ayimaqin-Kunlun-Mutztagh Suture; ALB = Alxa Block; HTG = Hetao Garben; LMSF = Longmenshan Fault; NCC = North China Craton; ODB = Ordos Block; QLO = Qilian Orogen; SCB = Sichuan Basin; SGT = Songpang-Ganzi Terrane; WQO = Western Qinling Orogen; YCG = Yinchuan Garben; NQS = North Qilian Suture; SQS = South Qilian Suture.

## 2. Method and Data Processing

### 2.1. Beamforming Theory

Beamforming consists of correcting recordings at N stations for the phase of a plane wave, summing over the stations and calculating the energy of the resulting beam. The energy of the beam $b(\omega, c, \theta)$ can be written (Ruigrok et al., 2017):

$$b(w,s,\theta) = \left| \sum_{p=1}^{N} v_p(\vec{r}_p,\omega) e^{-i\omega s \vec{r}_p \cdot \hat{e}_\theta} \right|^2, \tag{1}$$

where $\omega$ is frequency, $s$ is the slowness, and $\theta$ is the azimuth. Complex-valued $v_p$ is the record in the frequency domain at station $p$, whose coordinate relative to the average position of the array is denoted by $\vec{r}_p$. $\hat{e}_\theta$ is the unit vector of the wave number in azimuth $\theta$. Equation (1) can be recast into

$$b(w,s,\theta) = \left( \sum_{p=1}^{N} v_p(\vec{r}_p,\omega) e^{-i\omega s \vec{r}_p \cdot \hat{e}_\theta} \right) \left( \sum_{q=1}^{N} v_q(\vec{r}_p,\omega) e^{-i\omega s \vec{r}_p \cdot \hat{e}_\theta} \right)^* \tag{2}$$

or

$$b(w,s,\theta) = \sum_{p,q} e^{-i\omega s \vec{r}_p \cdot \hat{e}_\theta} (v_p v_q^*) e^{i\omega s \vec{r}_p \cdot \hat{e}_\theta}, \tag{3}$$

where we recognize the cross-spectral density matrix in the central term $v_p v_q^*$, the element that is used in traditional noise interferometry.

We calculate energy in the beam by first calculating the cross spectral density in the same way as in traditional interferometry, and then use it in equation (3). If the noise is coming from one dominant direction, we expect to get one single maximum in the beam energy map. If it comes from several directions, we expect several maxima at similar slownesses but different azimuths, and finally we expect a ring of maxima once noise is well distributed in azimuth (e.g., see Figure 1).

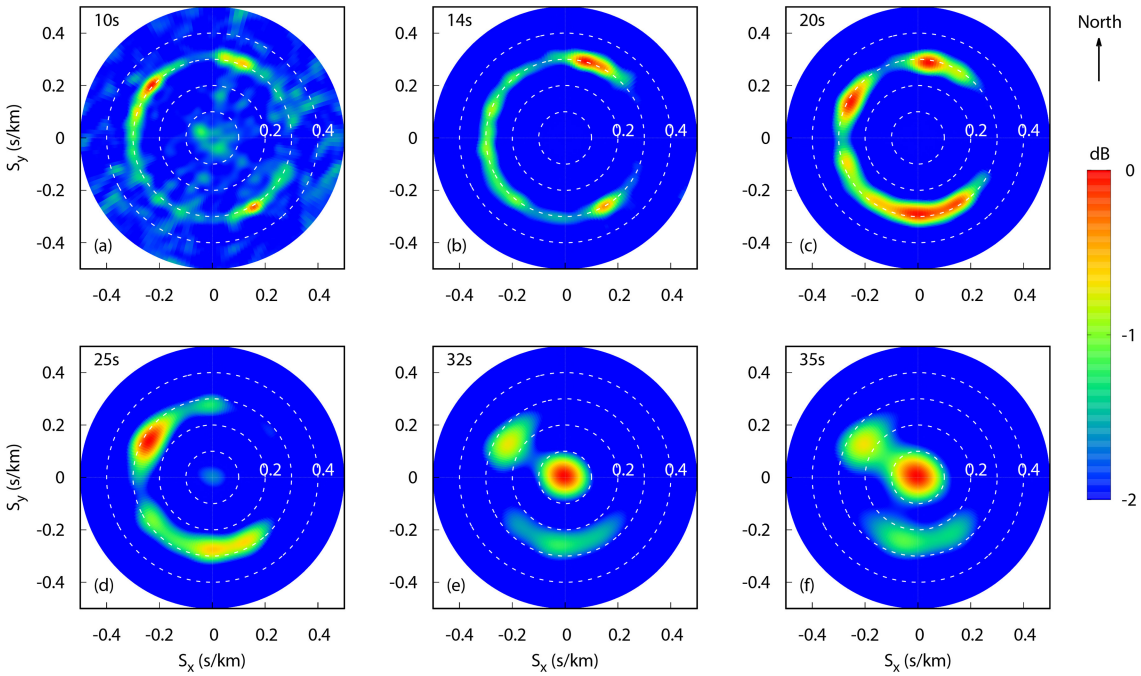


**Figure 2.** Energy spectrum as a function of slowness at six different periods for the $2^o \times 2^o$ grid cell shown in Figure 1 by a solid black frame. Forty-three stations are involved in this subarray.

As the distance to the noise sources is not known, we cannot correct for the curvature of the wavefront as we would have done when beamforming earthquake data, and we use a plane wave model in this study. According to Wathelet et al. (2008), the plane wave approximation is appropriate if the noise sources are distant from the array by at least 1.3 times the array diameter.

### 2.2. Data and Processing

In this paper, beamforming is applied to the noise recorded on the vertical components of 610 stations of the ChinArray (Phase II) network. ChinArray is a large observation project that aims to study the deep seismic structures and geodynamics of China by deploying a transportable seismic array. Multiphases are planned over the next 15–20 years, and 2-year observation is involved for each phase. ChinArray Phase II was operated from 2013 September to 2016 March. As shown in Figure 1, the phase II covers NETP with more than 670 stations and is the densest network so far in this area. The array features two kinds of stations: Guralp CMG-3ESPC with a corner period of 60 s and a CMG-3T with a corner period of 120 s, coupled with a Reftek 130 data acquisition system with a sampling rate of 100 Hz (Li et al., 2017).

Continuous waveforms were first decimated to one sample per second. According to the data processing procedures described by Bensen et al. (2007), for 1-day data, we first remove trend and mean, then divide the data into 1-h segments and apply one-bit normalization to limit the effect of transients like local or teleseismic earthquakes. We then cross correlate 1-h traces from two simultaneously recording stations, keep the cross-correlation traces from -700 to 700 s and stack them to obtain 1-day cross-correlation functions. Finally, all available day cross-correlations are stacked. As opposed to noise cross-correlation function studies, stacking over long periods of time is not required in noise beamforming analysis (Gerstoft & Tanimoto, 2007; Harmon et al., 2008; Roux & Ben-Zion, 2017), and we could have worked with shorter recording times or stacked less. We have no reason however to discard any data, and we have therefore chosen to stack all the data that are available to us. After quality control on the records, continuous records at 610 stations are finally used in this study.

Beamforming is performed on subarrays of $2^o \times 2^o$ dimensions, as illustrated in Figure 1 with a subarray example. We calculate the beam energy at 20 periods in the range 7 to 35 s using equation (3) after computing the cross-spectral density matrix for all the stations in the subarray by Fourier transform of the stacked cross-correlograms. Figure 2 shows the beam energy for the subarray shown by the black box in Figure 1, in which 43 stations are involved. It can be seen that the beam energy distribution is uneven in azimuth

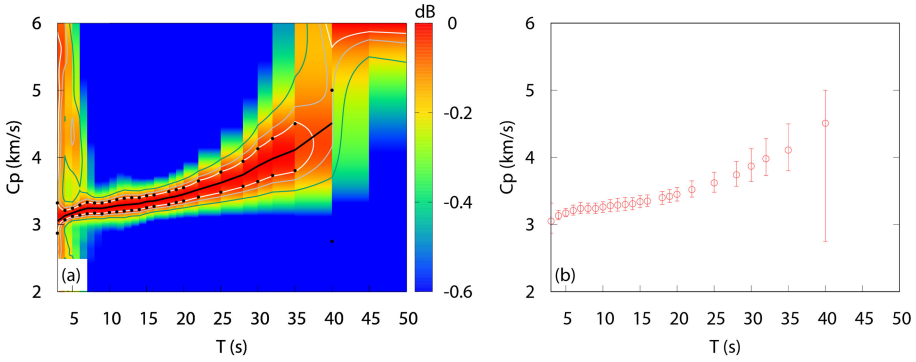


**Figure 3.** Illustration of the extraction of the azimuth-averaged phase velocity by beamforming the noise recorded by the stations located in the subarray labeled by a black box in Figure 1. (a) The azimuth-averaged beamforming output obtained by combining the results for all periods of interest, and transfer from period-slowness to period-velocity domain. (b) The phase velocity dispersion and error bars. The error bar is based on the bandwidth of ±0.99 maximum beamforming energy, called 0.99*EBW*.

due to a nonuniform distribution of the ambient noise source, but that a clear ring of energy stands out at up to 25 s period. At periods above 25 s, this ring, although still present, gets dominated by energy at zero slowness. This is due to the smaller amplitude of the ambient noise in this frequency range. The artefact at zero slowness is probably related to the data processing for a subarray with small aperture since our observations show that this artefact is moved to longer periods when beamforming data for arrays with larger aperture. This zero-slowness peak energy is excluded from further processing since it may bias the velocities at our longest periods towards too high values.

At each period, in order to get the azimuth-averaged beamforming result, we stack the beam energy with azimuth and then transform it to the velocity-period domain, as shown in Figure 3a. For each period, we search for the velocity corresponding to the maximum in the energy spectrum. This provides the average phase velocity of the fundamental mode Rayleigh wave at this period for the subarray. We evaluate the error in phase velocity using the width of the phase velocity range where energy is at 99% of the maximum (0.99*EBW*). As shown in Figure 3b, we finally get the dispersion curve of fundamental Rayleigh wave with uncertainties. The 0.99*EBW* or velocity error gets larger at long periods, indicating that resolution for average phase velocity degrades at long periods, due to the limitation of the array aperture.

Benefiting from the high density of stations, we obtain 2D phase velocity maps by applying this analysis on moving subarrays. As shown in Figure 4, the research area is parameterized by 2° × 2° grid cells with 0.5° overlap. For each cell, the beamforming method described above is used to calculate the phase velocity at different periods. This velocity is regarded as the average velocity of the cell, the reference coordinates of which are determined by averaging the coordinates over the stations inside the cell. The maps are produced

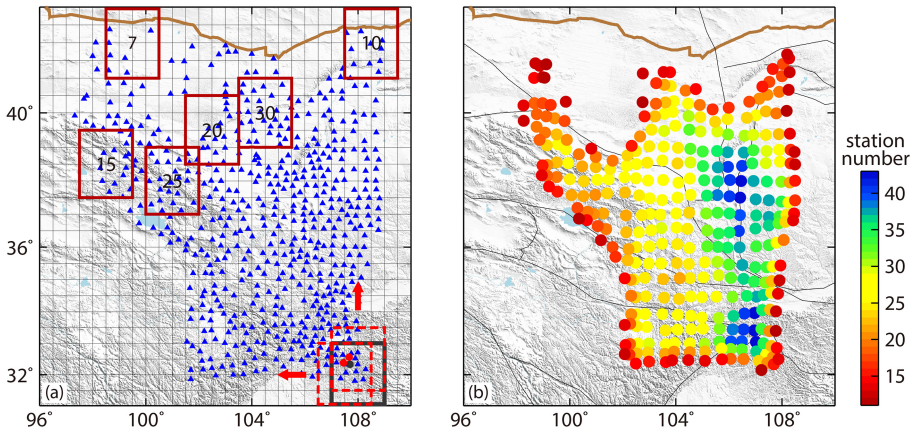


**Figure 4.** (a) Examples of subarrays with number of stations involved. The dispersion for the six subarrays shown by red solid frames is given in Figure 6. (b) Number of stations and reference location of the cells selected for data analysis.

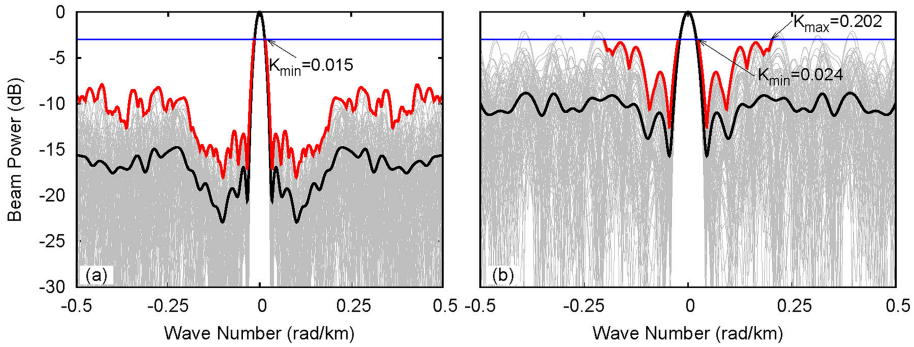


**Figure 5.** (a) Resolved wavenumber $K_{min}$ and $K_{max}$ for the subarray with 43 stations shown by a black box in Figure 1. (b) The same for the subarray with 10 stations shown with a red box in Figure 4. The gray lines denote the profiles of array response function (ARF) along the azimuth with $2^o$ step. The black line denotes the average over azimuth. The red line corresponds to the azimuth where the side lobe is nearest to the main peak. A -3dB line is denoted by the horizontal blue line. (see supporting information Figures S1 and S2 for the 2D distribution of ARFs)

by assigning the average velocity of the cell to the reference coordinates. All reference coordinates in the study area are shown by circles in Figure 4b. The color of the circles denotes the number of stations in the subarray and can be used to qualitatively assess the reliability of the velocity and resolution capability of the tomography result.

### 2.3. Beamforming Resolution and Phase Velocity Uncertainty

In choosing the dimension of the subarrays, we have to compromise between lateral resolution of the structure, benefiting from smaller arrays, and precision of the measurement, benefiting from larger arrays. Array performance for dispersion measurements from ambient noise have been studied by Wathelet et al. (2008). They show that the period range in which dispersion curves can be satisfactorily measured with an array can be evaluated by analysing its array response function (ARF). Figures 5a and 5b show the ARF for two subarrays of respectively 43 and 10 stations shown respectively in Figures 1 and 4. The gray lines display the profiles of the relative ARF in decibel for different azimuths every $2^o$ step, whereas the black solid line shows the azimuthal average. As the noise is not evenly distributed, the resolution in the present study is intermediate between the one-direction cases and the azimuthal averages.

Following Wathelet et al. (2008) and using the half-width of the main lobe at -3dB (denoted by a blue line) as the minimum wavenumber resolved, this yields a minimum wavenumber $k_{min} = 0.015$ km$^{-1}$ for the subarray with 43 stations and $k_{min} = 0.024$ km$^{-1}$ for the subarray with 10 stations, corresponding to periods of about 140 and 80 s respectively for a velocity of 3 km/s, which is well beyond the period range where we have signal in the ambient noise. This is similar to minimum wavenumber estimations using the method of Ruigrok et al. (2017) based on the dimension of the array.

Sidelobes crossing the −3 dB line indicate wavenumbers where severe aliasing occurs. Although aliasing would occur in single azimuths for the subarray with 10 stations, it does not affect the averaged kernels in the range of wavelengths used in this study.

Figure 6 shows the beam energy in the period-velocity domain for six examples of subarrays with different configurations and number of stations, as shown by red boxes in Figure 4a. For the subarrays with more than 10 stations, we observe that the results are stable and the dispersion curves smooth in the period range from 7 to 35 s, although the azimuthal distribution of station pairs may vary a lot from cell to cell. We observe also that the azimuth distribution of station pairs does not affect much the quality of the results since the surface wave dispersion is extracted from an azimuth-averaged result. This would of course be very different if we tried to retrieve the azimuthal anisotropy (Lu et al., 2018).

The error bars are not small and increase significantly beyond 25 s period. Their distribution in the study area can be seen in Figure 7. They correspond to about ±0.1 to ±0.25 km/s at $T = 10$ s and ±0.2 to ±0.4 km/s at $T = 25$ s for most of the study region. Interestingly, we can notice that the uncertainties do not reflect directly the number of stations in the subarrays. For example, the increased number of stations per subarray to the east (see Figure 4) does not lead to smaller error bars in the area. A spot located at around $36^oN-106^oE$

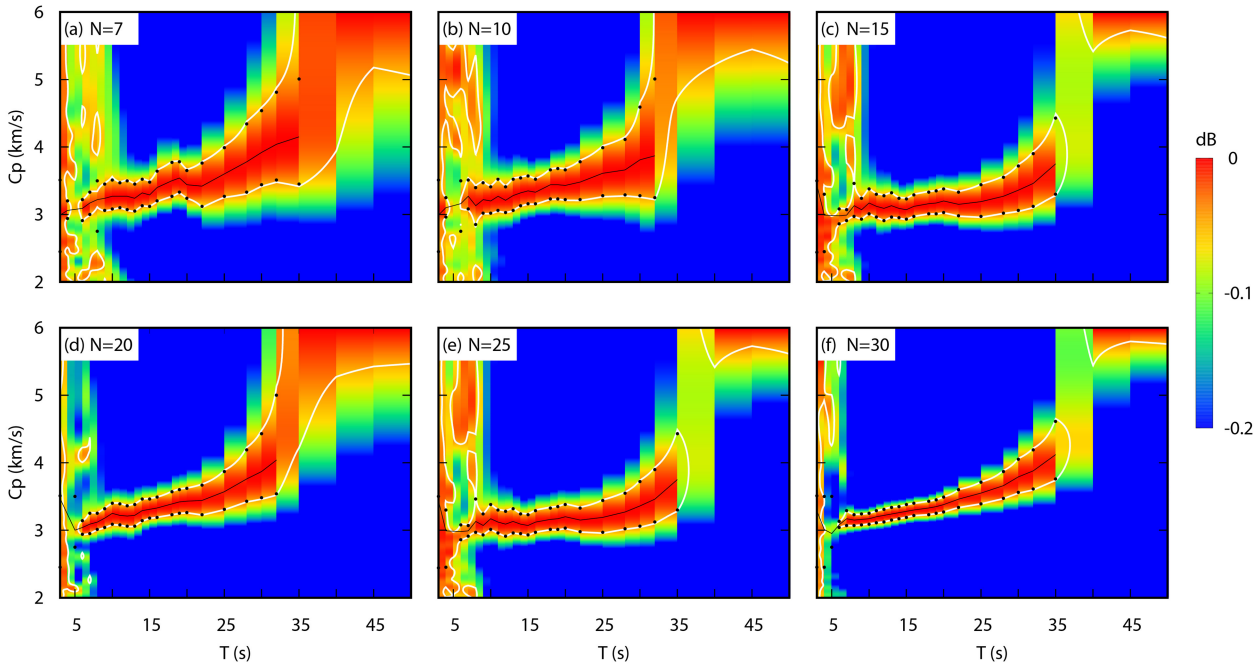


**Figure 6.** Dispersion measurement for the subarrays shown in Figure 4a with a number of stations ranging from 7 to 30. Black lines are phase velocity dispersion curve of the Rayleigh wave fundamental mode corresponding to the maximum of energy spectrum, and black dots are velocity error bars computed by 0.99*EBW*.

shows particularly large error bars at all periods despite the large station density in the area. This might be related to a disruption of the wavefield in this location due to a more complex underlying structure.

Considering the limitations related to beamforming at small subarrays, as discussed above, we opted for beamforming on a grid of cells with $2^o \times 2^o$ dimensions with $0.5^o$ overlap between neighboring cells. Only cells with at least 10 stations were used (see Figure 4b for number of stations map). Although the dimensions of the subarrays limit the resolution to about 200 km, we deem that smaller subarrays would lead to too high uncertainty in the measurements. Roux and Ben-Zion (2017) use in Southern California subarrays of half the dimension of ours and indicate that this leads to an uncertainty of ±0.3 km/s, which is consistent with our results.

The optimal subarray dimension found here is of course intimately linked to the goal of the study, which is to image the crust. For more general studies, an adaptive grid size could be used to provide higher resolution at shorter periods to map the shallow structure and precise enough information at longer periods to constrain the deeper structure, although at the expense of poorer lateral resolution at depth.

## 3. Phase Velocities

### 3.1. Rayleigh Wave Phase Velocity Maps

Figure 8 shows the 2D phase velocity maps of Rayleigh waves obtained at six different periods. Although comparison with the tectonics of the area is postponed to the discussion of the S-wave velocity model in section 4, we can note here that the velocity distribution at 10 s reflects well the presence of sedimentary basins to the northeast (at the boundary between the Ordos Block, the Hetao Graben, and the Yinchuan Graben) as well as the presence of exposed metamorphic rock and granite in the southeastern part of the region, characterized by high velocities. At longer periods, the main feature common to all maps is clearly a west/southwest-east/northeast dichotomy with low velocities to the west and high velocities to the east. We can also note a rather unusual feature in our phase velocity maps: the amplitude of the lateral variations increases with period, from 9% to 13% and then 25% at respectively 10, 20, and 30 s periods. This feature can be related to the large increase in crustal thickness from 40 to 65 km from east to west in the area (e.g., Wang et al., 2017a), which is expected to produce large phase velocity variations in our longest period range. The main features in our maps, including the amount of lateral variability at the different periods, are in very good agreement with the Rayleigh wave phase velocity maps produced by Yang et al. (2010) with classical

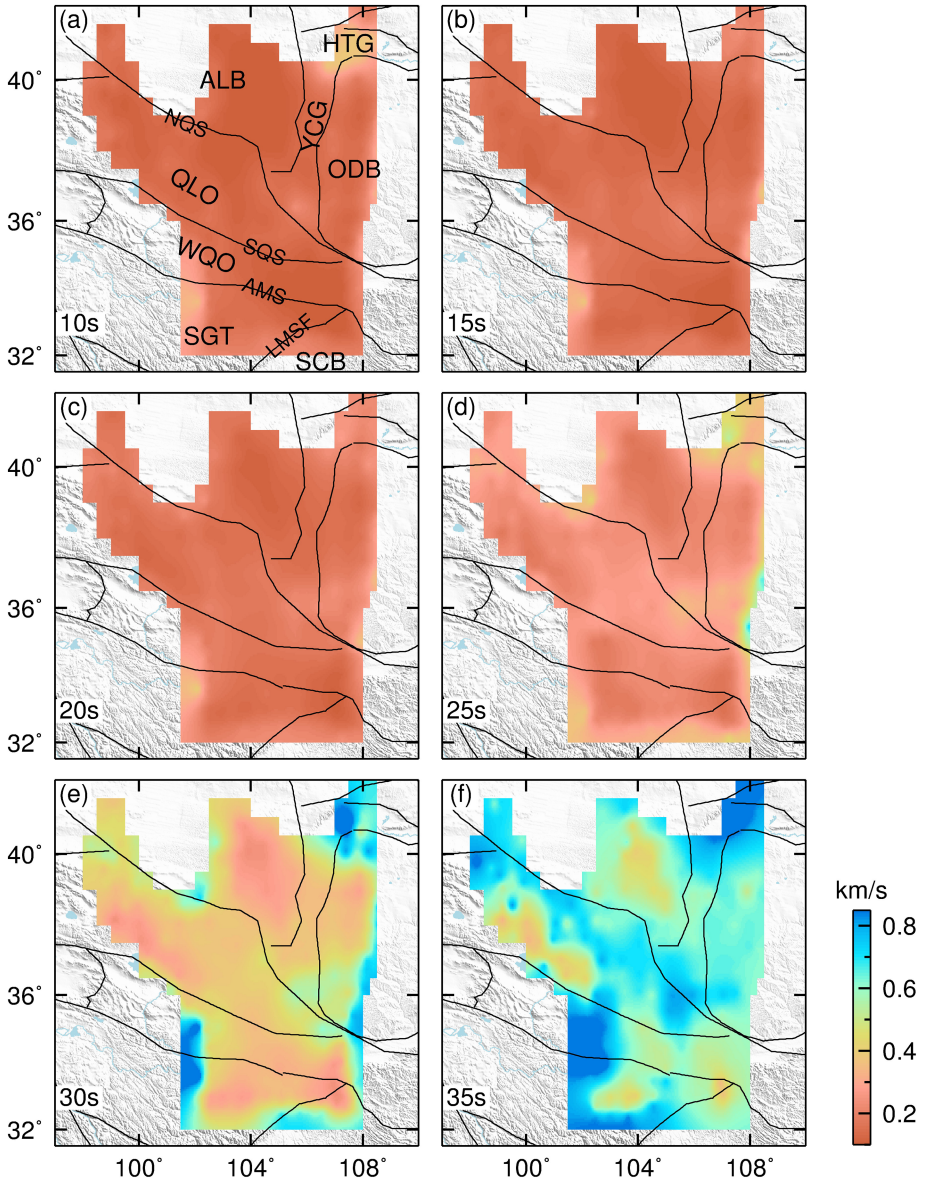


**Figure 7.** Estimated errors maps for phase velocities at periods of 10, 15, 20, 25, 30 and 35 s.
AMS = Ayimaqin-Kunlun-Mutztagh Suture; ALB = Alxa Block; HTG = Hetao Garben; LMSF = Longmenshan Fault; NCC = North China Craton; ODB = Ordos Block; QLO = Qilian Orogen; SCB = Sichuan Basin; SGT = Songpang-Ganzi Terrane; WQO = Western Qinling Orogen; YCG = Yinchuan Garben; NQS = North Qilian Suture; SQS = South Qilian Suture.

ambient noise tomography. Note that their study is at a scale larger than ours and covers the whole of Tibet and adjacent areas.

### 3.2. Comparison With Other Methods

Figure 9 shows a comparison of our results with those of two studies presently available on Rayleigh wave phase velocity using data from the ChinArray II network. The left column (a, d, and g) are the results obtained by the beamforming method presented in this study. The middle column (b, e, and h) is generated using the eikonal equation applied on earthquake data by Zhong et al. (2017). The right column (c, f, and i) is the tomography results by pure-path inversion of surface wave dispersion of earthquake data (Li et al., 2017).

In general, we observe a good degree of similarity between the maps produced by the three methods. At periods of 12 and 20 s, the velocity difference between eikonal tomography and beamforming method is

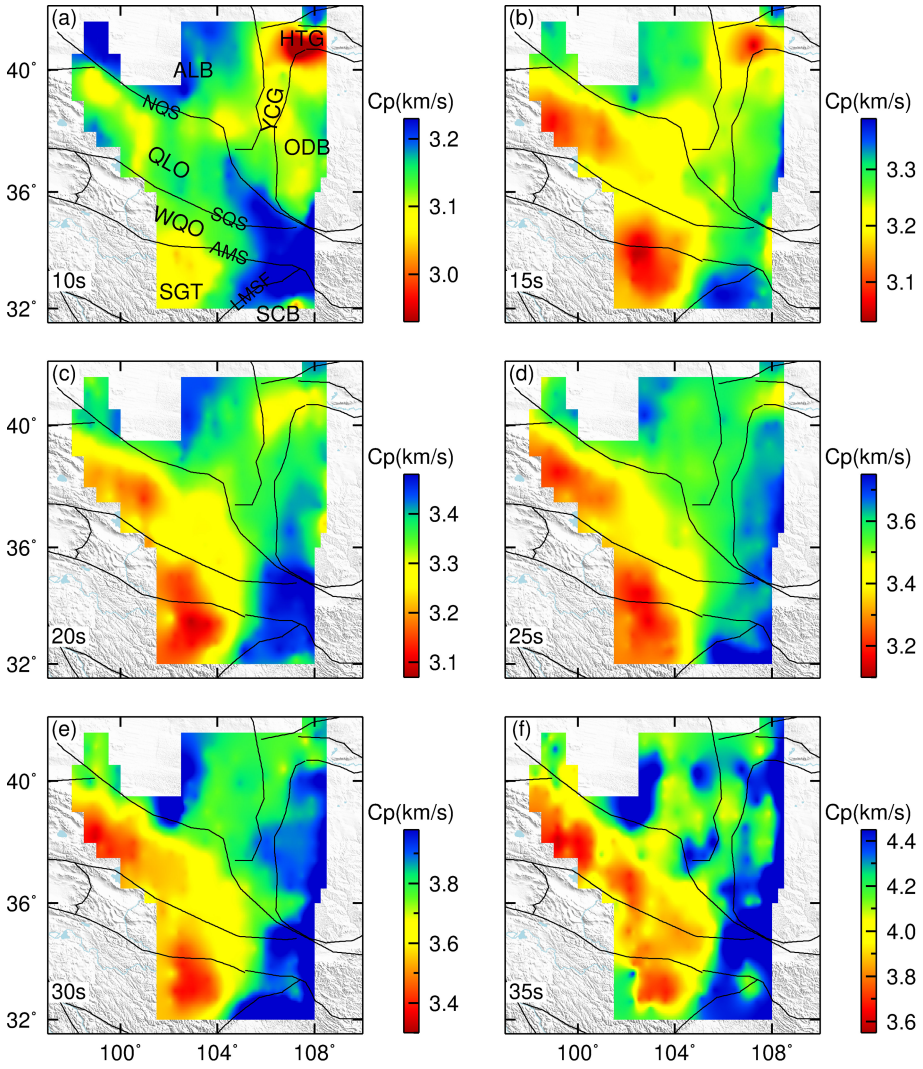


**Figure 8.** Estimated phase velocity maps at periods of 10, 15, 20, 25, 30 and 35 s. The spread in phase velocities across the study region is respectively 9%, 11%, 13%, 22%, 25%, and 32% from 10 to 35 s period.
AMS = Ayimaqin-Kunlun-Mutztagh Suture; ALB = Alxa Block; HTG = Hetao Garben; LMSF = Longmenshan Fault; NCC = North China Craton; ODB = Ordos Block; QLO = Qilian Orogen; SCB = Sichuan Basin; SGT = Songpang-Ganzi Terrane; WQO = Western Qinling Orogen; YCG = Yinchuan Garben; NQS = North Qilian Suture; SQS = South Qilian Suture.

±0.1 km/s for most of the research region, which is within the uncertainty of our results. At 12 s period, the phase velocity produced by beamforming (Figure 9a) has a larger wavelength structure than the map produced by eikonal tomography (Figure 9b), which has more small scale details. This is probably due to the fact that the eikonal tomography is based on a very local evaluation of the phase gradient that has the potential for resolving smaller features. Compared to eikonal tomography, beamforming is also a localized measurement but operates at the larger scale of a subarray. Although this smoothes the structure, the fact that each measurement is based on a larger number of phase data may increase the robustness of the result and decrease errors in larger scale features. The map produced with the pure-path method (Figure 9c) features stronger contrasts with less small scale details than the other maps, which might be due to the fact that surface waves from distant earthquakes at these short periods often show interference patterns difficult to exploit with traditional pure-paths methods.

The degree of similarity between the three methods is very high at 20 s period. The eikonal tomography also shows more small-scale details at these periods, but the large wavelength patterns are now similar to the ones obtained with beamforming. Pure-path results still show larger contrasts but less small-scale details.

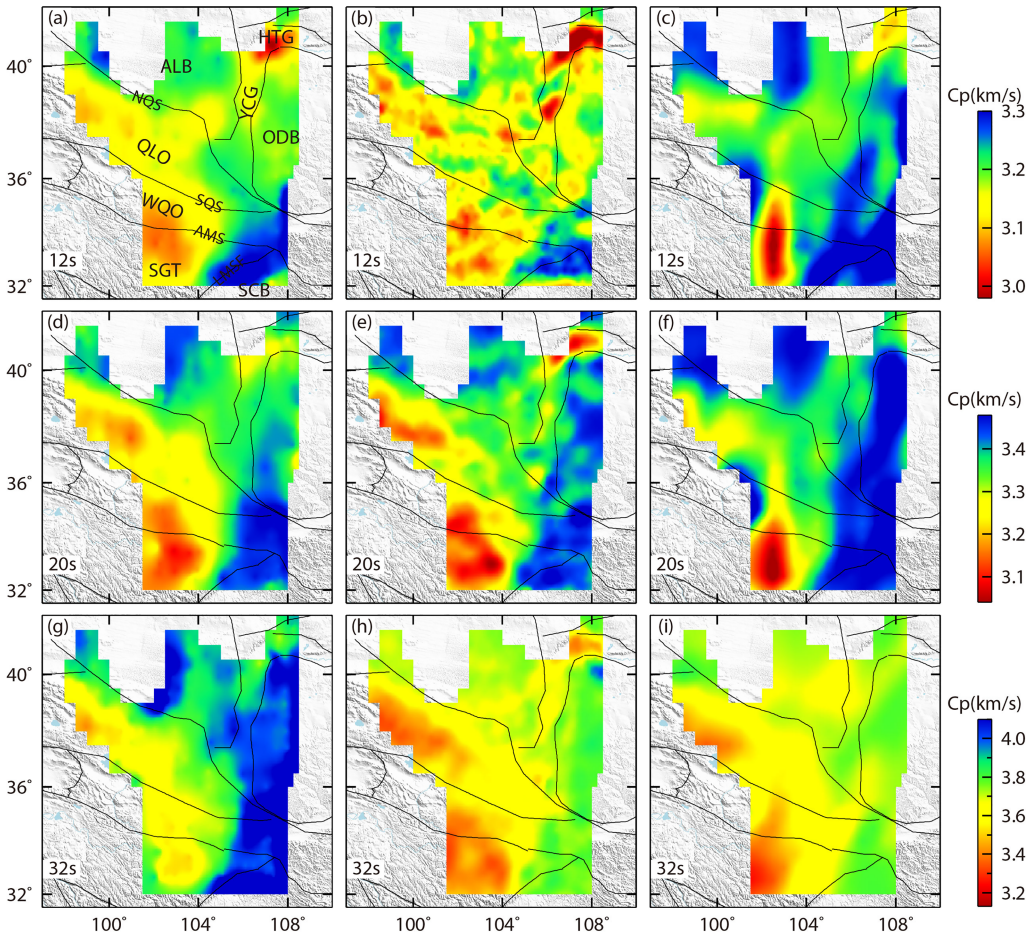


**Figure 9.** Phase velocity maps obtained by three methods at periods of 12, 20, and 32 s. The left column (a, d, and g) are the results of this study. The middle column (b, e, and h) are the results obtained by eikonal tomography of earthquake events (Zhong et al., 2017). The right column (c, f, and i) are the results obtained by traditional surface wave tomography of earthquake data (Li et al., 2017). AMS = Ayimaqin-Kunlun-Mutztagh Suture; ALB = Alxa Block; HTG = Hetao Garben; LMSF = Longmenshan Fault; NCC = North China Craton; ODB = Ordos Block; QLO = Qilian Orogen; SCB = Sichuan Basin; SGT = Songpang-Ganzi Terrane; WQO = Western Qinling Orogen; YCG = Yinchuan Garben; NQS = North Qilian Suture; SQS = South Qilian Suture.

At 32 s period, our results show a similar pattern of lateral heterogeneity but higher velocities than the two other methods, which show very similar results. Although the fast anomaly to the southeast of our study region is obtained with subarrays with few stations and could therefore be questionable, it fits very well with the high velocities in the other maps and a very high velocity region found in the Sichuan Basin by the larger scale noise interferometry study of Yang et al. (2010). The higher average value in our results may be due the fact that ambient noise amplitude decreases at this period and that our measurements get biased by interference with processing-related zero-wavenumber energy (Figure 2). The main drawback of our method and of any local method is that information contained in longer paths is discarded, which particularly disadvantages longer periods. This could been mitigated by using larger subarrays at longer periods or combining beamforming with traditional interferometry. As the main focus of this study is crustal structure, we will not implement this strategy here and simply refrain from interpreting mantle velocities.

## 4. S-Wave Model

### 4.1. Depth Inversion

Combining the phase velocity at different periods for each subarray, a dispersion curve can be obtained for each reference point. A 3D shear-wave velocity model can then be established by fitting the dispersion curves at the reference points through a depth inversion algorithm.

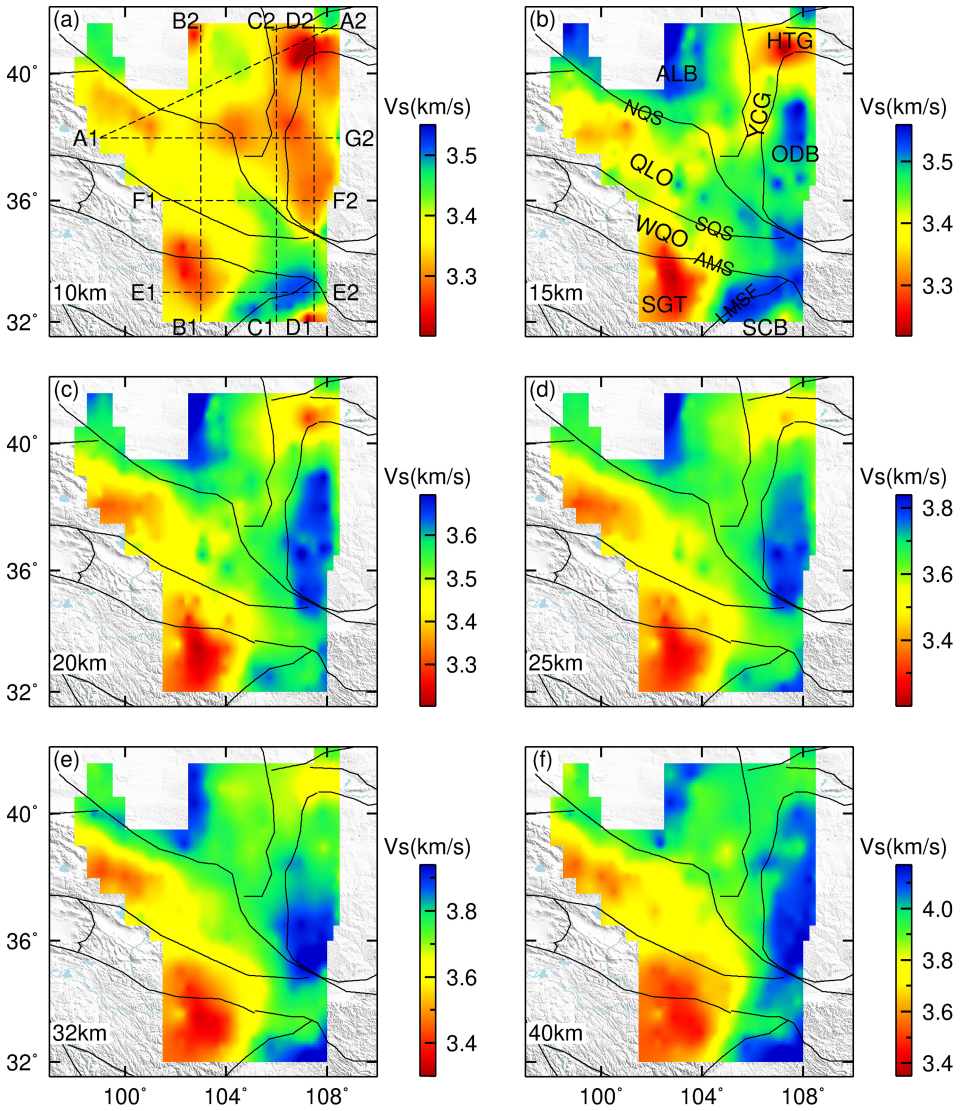


**Figure 10.** Shear wave maps at depths of 10, 15, 20, 25, 32, and 40 km. The lines in Figure 10a denote the location of the vertical profiles shown in Figure 11. AMS = Ayimaqin-Kunlun-Mutztagh Suture; ALB = Alxa Block; HTG = Hetao Garben; LMSF = Longmenshan Fault; NCC = North China Craton; ODB = Ordos Block; QLO = Qilian Orogen; SCB = Sichuan Basin; SGT = Songpang-Ganzi Terrane; WQO = Western Qinling Orogen; YCG = Yinchuan Garben; NQS = North Qilian Suture; SQS = South Qilian Suture.

As the depth of major interfaces is not well resolved with surface waves and can easily lead to trade-off with velocities, we choose to fix the Moho depth to values obtained in the same area with receiver functions (Wang et al., 2017b). Except for this fixed discontinuity, and in order not to impose a predefined structure either to the crust or the mantle through a layered parametrisation, we adopt an inversion procedure that allows for continuous variations with depth of the parameters. The iterative linearized inversion (Tarantola & Valette, 1982) follows a procedure used in Lévêque et al. (1991) and Maupin and Cara (1992) and refined in Maupin (2011).

An essential point in the procedure is the control of the smoothness of the model variations with depth by an a priori correlation function that partly couples the variations of the parameters at different depths through nondiagonal terms in the model a priori covariance matrix $C_m$. We use Gaussian correlation functions with an increasing correlation length with depth (Maupin, 2011), reflecting that we expect to be able to resolve more details close to the surface than further down. The a priori covariance between the model parameters

at two depth-points $z_1$ and $z_2$ is expressed as follows:

$$C_m(m(z_1), m(z_2)) = \sigma_m^2 exp(-(z_1 - z_2)^2/(2L(z_M)^2)), \quad (4)$$

where the correlation length $L$ is a chosen function of $z_M$, the mid-point between $z_1$ and $z_2$, and $\sigma_m$ is the a priori standard deviation of the model parameters. We choose $\sigma_m$ to be 0.25km $s^{-1}$ and $L$ to increase linearly from 10 km at the surface to 30- at 200-km depth.

The initial model is a combination of AK135 mantle model and crust 1.0 (Kennett et al., 1995; Laske et al., 2013), where the Moho depth is modified by the results obtained by Wang et al. (2017b) using receiver functions. Only the shear wave velocity is inverted. P-wave velocity and the density are kept at their initial model values. We preformed five iterations, but the inverted results were stable after the first one. We also check that our inversion results do not depend on our choice of Moho depth by comparing our final results with results obtained with different Moho models in the area (see supporting information Figures S3 and S4).

### 4.2. Characteristics of the S-Wave Velocity Model

Combining the 1D velocity profiles of each reference point, we produce a 3D shear wave velocity structure in NE Tibet and adjacent area. The inverted shear wave velocity model is shown as maps at depths of 10, 15, 20, 25, 32, and 40 km in Figure 10 and as vertical sections in Figure 11. Figure 12 shows the a posteriori error estimation of the depth inversion. The gray band area in (a) and (c) shows the a posteriori error estimation of the 1D S-wave velocity profiles which are located at the grid denoted by the dashed lines in (b) and (d), respectively. Panels (b) and (d) shows respectively the a posteriori error along the sections A1–A2 and B1–B2.

From a tectonic point of view, the study region can be divided into two main units: The northeast part consists of two cratonic blocks, Alxa Block and Ordos Block, separated by Yinchuan and Hetao Graben. The southwestern part forms the northeast margin of the Tibetan Plateau and consists of three orogenic units with high elevation, Qilian Orogen (QLO), Western Qinling Orogen, and Songpan-Ganzi Terrane (SGT), separated by major faults. At the southeast corner of our study region, we enter the Sichuan Basin.

At 10-km depth (Figure 10a), the velocities are lowest to the northeast, reflecting thick sedimentary deposits of about 10 km thickness, especially in the Hetao Graben (Wang et al., 2017b). The low velocities of 3.2 km/s observed at 15 km are probably due to vertical leakage of the structure of the sedimentary basins above. Note that the a posteriori errors in the upper crust are at their largest in this area, at about 0.2km/s (Figure 12b). To the southwest, the Western Qinling Orogen and Songpan-Ganzi Terrane are also characterized by low-velocity anomalies at 15-km depth. As the Cenozoic sediments in the intermontane basins of this area, such as the Zoige Basin, are less than 3 km thick (Wang et al., 2017b), leakage from sedimentary layers is more unlikely in this region, and we interpret these low velocities as real mid-crustal low-velocity anomalies. By contrast, the eastern corner of the plateau has relatively high velocities between 3.45 and 3.5 km/s. The mountainous regions in the vicinity of Longmenshan Fault in the southeast corner are in particular characterized by high velocity of more than 3.5 km/s, which can be related to the presence of metamorphic rock and granite exposed at the eastern part of this Orogen.

Except for a general slight increase of the average velocity with depth, the maps are very similar from 20- to 40-km depth. The Hetao graben retains a low-velocity signature, which can be related to trade-off between very thick sediments at the surface and deeper crustal structure. The main feature otherwise is the difference between the high velocities in the cratonic blocks and associated grabens compared to the low velocities beneath the Tibetan Plateau. The boundary between high and low velocity follows the north and eastern edge of the Plateau quite well up to 105° east, where it turns southwards, cutting across the tectonic units. The generally low-velocity region at the NE margin of Tibet has consistently with depth two isolated anomalies with even lower velocities. One in located to the northwest of the QLO and the other one in the SGT). This agrees well with the result of Li et al. (2017).

Figure 11 shows vertical sections of shear wave velocity profiles for lines shown in Figure 10a, with west-east sections to the left and north-south sections to the right of the Figure.

Both lateral and vertical variations of S-wave velocity are well seen on the vertical profiles. In the Songpan-Ganzi terrane beneath the high-topography areas of NETP, a clear low-velocity zone (LVZ) is prominent at 15-to 35-km depth (sections B1–B2 and E1–E2), with a minimum velocity lower than 3.25 km/s in the middle of the crust. This minimum is also well seen in the 1D S-wave velocity profile around SGT

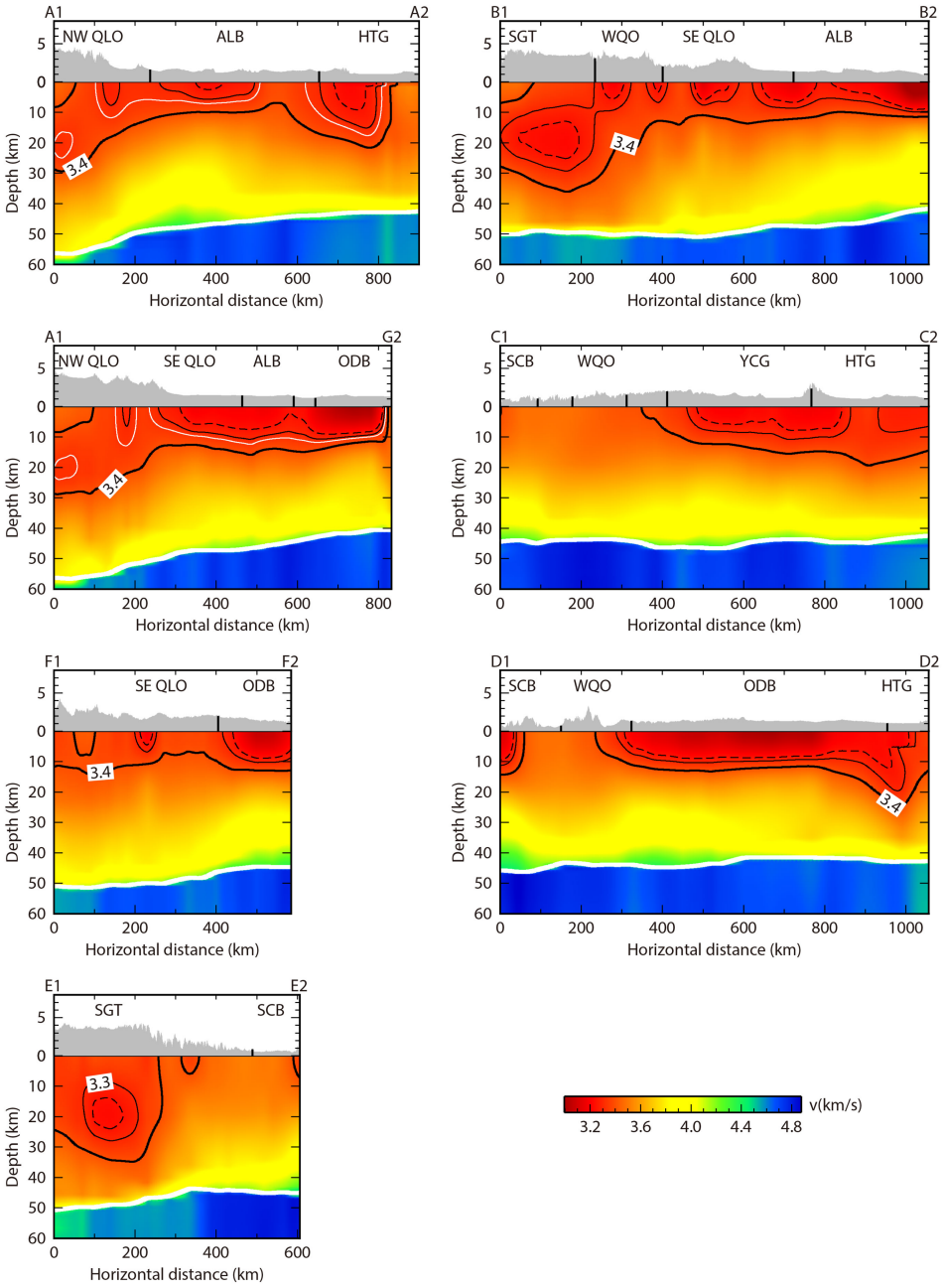


**Figure 11.** Cross-sections of shear wave velocity along lines shown in Figure 10a. Black dashed lines are velocity at 3.25 km/s. Black solid lines are velocity at 3.3 and 3.4 km/s. White lines are Moho interface obtained by receiver function by Wang et al. (2017b). All depth are relative to sea level. ALB = Alxa Block; HTG = Hetao Garben; NW = northwest; ODB = Ordos Block; QLO = Qilian Orogen; SE = southeast; SCB = Sichuan Basin; SGT = Songpang-Ganzi Terrane; WQO = Western Qinling Orogen; YCG = Yinchuan Garben.

in Figure 12c. The red line in Figure 12c denotes the reference velocity $V_{ref}$ = 3.4km/s used in the following section to quantify the presence of LVZ. The a posteriori errors at 20 km depth are about 0.13 km/s (Figure 12), indicating that the presence of the LVZ in SGT is well contrained by our data. Further north, on profiles A1–A2 and A1–G2 beneath the Northwestern QO, another slightly less pronounced LVZ can also be observed at mid-crustal depths.

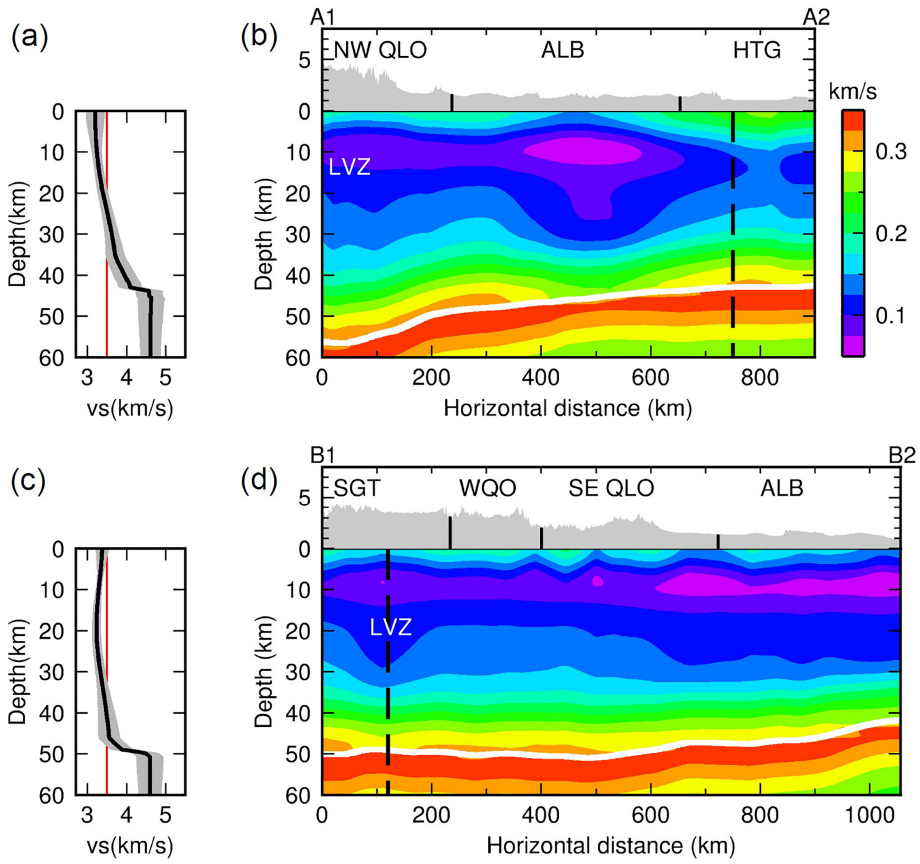


**Figure 12.** A posteriori error estimation of the depth inversion. The gray band area in (a) and (c) shows the a posterior error estimation of the 1D S-wave velocity profiles which are located at the grid denoted by the dashed lines in (b) and (d), respectively. The red line in (a) and (c) denotes the reference velocity $V_{ref}$ = 3.4km/s, which are used in equations (5) and (6) to quantify the presence of LVZ. Panels (b) and (d) show respectively the a posteriori error along the sections A1–A2 and B1–B2. White lines are Moho interface obtained by receiver function by Wang et al. (2017b). All depth are relative to sea level. ALB = Alxa Block; HTG = Hetao Garben; LVZ = low-velocity zones; NW = northwest; ODB = Ordos Block; QLO = Qilian Orogen; SE = southeast; SCB = Sichuan Basin; SGT = Songpang-Ganzi Terrane; WQO = Western Qinling Orogen.

The low velocity to the east in the A1–A2 profile deeper than 10 km may result from trade-off with the thick sedimentary basins above. Except for the prominent low velocities discussed above, the structure of the crust in the study region is rather normal. The velocities are not significantly different from the velocities of respectively 3.46 and 3.85 km/s in the upper and lower crust of the standard continental crustal part of model AK135F (Kennett et al., 1995). This reflects that the ODB, as the west part of North China Craton, is an ancient and stable continental block. The normal velocity distribution from the Central ODB to the Northern Sichuan Basin shows a stable mid-crust whereas the low velocities in the NE margin of Tibet are characteristic of active mid-crust.

### 4.3. Tectonic Implications of the Crustal LVZ

It is generally considered that vertically localized low shear-wave velocity layers in the crust result from partial melting or existence of fluids. Experimental geophysics has suggested that partial melt or aqueous fluids in the crust can absorb elastic wave energy and cause velocity reduction, contributing to mechanically weak zones, limiting accumulation of strain energy. These zones are characterized by low shear wave velocity, high conductivity, and high surface heat flow (e.g., Bao et al., 2015; Liu et al., 2014; Wang et al., 2017a; Zhan et al., 2014). As LVZs are associated with potential for crustal channel flow, their delineation can provide constraints for crustal flow models and give a further understanding of the crust-mantle structure and deformation mechanism in NE Tibet. Two middle-crustal LVZs, located at the Northwestern Qilian Orogen (NW QLO) and SGT, are the most prominent and interesting features of our 3D S-wave velocity model, and we will now analyze them in further details.

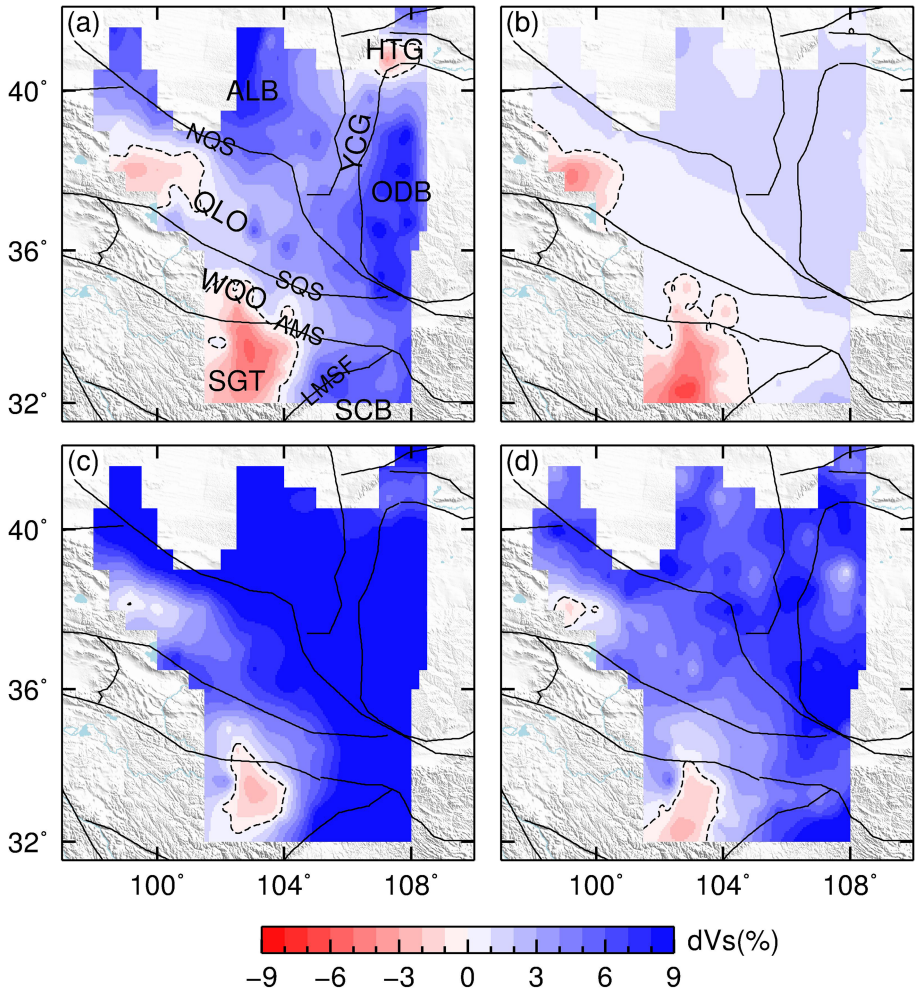


**Figure 13.** (a) Map of the amplitude of the LVZ based on equation (5) at 20-km depth (relative to sea level).(b) Same as (a), but with the definition given by equation (6). The contour with dashed lines denotes the boundary of the LVZ, where the velocity is equal to the reference one. Panels (c) and (d) are correspondingly the same as (a) and (b) but at the depth of 30 km (relative to sea level). AMS = Ayimaqin-Kunlun-Mutztagh Suture; ALB = Alxa Block; HTG = Hetao Garben; LMSF = Longmenshan Fault; ODB = Ordos Block; QLO = Qilian Orogen; SCB = Sichuan Basin; SGT = Songpang-Ganzi Terrane; WQO = Western Qinling Orogen; YCG = Yinchuan Garben; NQS = North Qilian Suture; SQS = South Qilian Suture.

#### 4.3.1. Delineation of LVZs

Yang et al. (2012) defines two ways of quantifying the presence of a crustal LVZ. The first one simply calculates at a given depth $z_0$ the relative deviation with respect to a reference value $V_{ref}$, which can be for example the velocity at which partial melt is expected to occur.

$$\mathrm{LVZ}_1 = \frac{V(z_0) - V_{ref}}{V_{ref}} \tag{5}$$

LVZs are simply regions where this quantity is negative.

The second definition expressed by equation (6) identifies regions with a vertically localized minimum shear wave velocity beneath the upper crust by calculating

$$\mathrm{LVZ}_2 = \frac{V(z_0) - V_{\max}(0 - 18 \quad \mathrm{km})}{V_{ref}}. \tag{6}$$

$V_{\max}(0 - 18 \quad \mathrm{km})$ denotes the maximum shear wave velocity between the surface and 18-km depth, this depth being chosen here to represent the lower possible depth of the upper crust in our area. Again, LVZs

are regions where this quantity is negative. We choose $V_{ref} = 3.4$km/s as in Yang et al. (2012), where they argue that this velocity is appropriate to delineate partial melt occurring in crustal metamorphic rocks at 30 km depth.

We use these two equations at two different depths, 20 and 30 km. Compared with Yang et al. (2012) who use only 30-km depth, we add the 20-km depth case because our study area covers a part outside Tibet where the crust is thinner. Moreover, the section profiles A1A2, B1B2, and A1G2 in Figure 11 show that the lowest value of the velocity appears at a depth of 20 km instead of 30 km in our area. Independent data from deep seismic sounding also show that a significant low velocity in the Songpang-Ganzi Terrane appears at around 20-km depth (Liu et al., 2006). Considering that the shear wave velocity in the lower crust is usually not considered as increasing significantly with depth, and taking into account the uncertainty in the velocity characterising melt onset, we use the same reference velocity value at 20- and 30-km depth.

Figure 13 shows the LVZs according to equations 5 and 6 at 20-km depth (plots a and b), and 30-km depth (plots c and d). The contour with dashed lines denotes where the velocity is equal to the reference one. At 20 km depth, two LVZs are clearly observed at NW QO to the northwest and SGT to the south with both LVZ definitions. The LVZ according to equation (5) has an amplitude of -6% in SGT and −3% in NW QO, whereas the amplitude grows to −9% in SGT and −5% in NW QO for the definition in equation (6), showing that in both cases, the vertical heterogeneity is larger than the horizontal one. At a depth of 30 km, the LVZ in the NW QO is almost nonexistant, in accordance with the results of Yang et al. (2012) who place this region at the eastern border of a LVZ. In the SGT, we find a LVZ of −3%, weaker than at 20-km depth. Yang et al. (2012) also place this region at the border of a strong LVZ, whereas Li et al. (2014a) find LVZs of respectively −2% and −5% in these two regions.

#### 4.3.2. The LVZ and the East Kunlun Fault

Crustal flow models predict that excess topography will drive a flow outwards from the Plateau in the presence of crustal weak layers (Clark & Royden, 2000; Jiang et al., 2014). East of the Tibetan Plateau and more precisely around the SGT, an important question to constrain the crustal flow and the dynamic evolution of Tibet is the origin and role of the East Kunlun Fault (Ayimaqin-Kunlun-Mutztagh Suture), and in particular whether or not the flow has a northeastward branch that crosses this fault due to the possible blocking to the east by the Sichuan Basin.

In our model, the LVZ in the SGT extends at 20-km depth about 100 km northward of the East Kunlun Fault (Figure 13). The velocity from beamforming analysis is an average value over $2^o \times 2^o$ areas. The reference point of the first subarray located fully north of the fault is therefore at about 100 km from the fault itself. Considering that the velocity at this point is not above the reference velocity, at it would be in a normal crust, we infer that the LVZ in SGT crosses the East Kunlun Fault. This is consistent with Jiang et al. (2014) where the LVZ distribution in SGT penetrates northward into East Kunlun Fault but is slightly different from Li et al. (2014a) who suggest that East Kunlun Fault is the north boundary of the mid-crustal LVZ in SGT.

In their interpretation of the Kunlun fault, in particular in its relation to the northern boundary of the LVZ, Li et al. (2014a) also use the same equations 5 and 6 at a depth of 30 km but with a reference velocity of 3.45 km/s. Note that all other factors being identical, this larger reference velocity should lead to a larger LVZ compared to our results and those of Yang et al. (2012). In our model, the boundary of the LVZ gets closer to the East Kunlun Fault at 30-km depth, and the LVZ amplitude in SGT becomes weaker north of the Kunlun fault. The resolution does not allow a definitive answer as to whether the LVZ extends north of the Kunlun fault or not at that depth. From our results, it seems however that the LVZ is stronger at more shallow depth and that results at 30-km depth may underestimate the extent of the LVZ.

#### 4.3.3. The Origin of the Low Velocities

Low shear wave velocities in the crust are usually attributed to the presence of partial melts or fluids, which should also results in high Poisson's ratios and high electric conductivity (Bendick & Flesch, 2007). Although it is of course not possible from our study alone to discriminate between the different tectonic processes able to induce melts or fluids in the crust of the NETP, we discuss shortly here how our study may bring constraints to the different possible options in the two regions where we observe LVZs.

In the SGT, where we have the strongest LVZ, slightly higher Poisson's ratio of about 0.28 (Wang et al., 2017a) has been found, as well as high electric conductivity. Li et al. (2017) suggest that the partial melting in SGT results from asthenospheric upwelling by delamination of a thick lithosphere root. Wang et al. (2017b) indicate that in addition to the localized asthenosphere upwelling, shear heating due to the relative movement

between Western Qinling Orogen and Songpang-Ganzi Terrane and crustal radioactivity from the thickened crust (Jiang et al., 2014) may contribute. Pan et al. (2017) suggested that mid-crustal partial melting in SGT may not be as large-scale as in Southeast Tibetan Plateau since Poisson's ratio is not much higher than the global average and low surface heat flow is observed. This is also supported by our results, since we find LVZs of moderate amplitude, where additional heat from shear heating is not required. The absence of LVZ in our model in the Western QO, despite the presence of major faults, is also in disfavor of shear heating being a major source for partial melting.

In NW QO, where we find a weaker LVZ, Jiang et al. (2014) observes a mid-crustal LVZ comparable to the one they find within the SGT and attribute this LVZ also to partial melting. Lower electrical conductivity (e.g., Zhan et al., 2014; Zhao et al., 2015) and Poisson's ratio <0.23 (Wang et al., 2017a) are observed in NW QO. This means partial melting may not occur in this region. Pan et al. (2017) and Li et al. (2017) suggest that the LVZ in NW QO relates to aqueous fluids in consideration of the maximum conductivity being approximately equal to the one of aqueous fluids. They propose that mid-crustal LVZs may be at brittle-to-ductile transition and act as a mechanical trap for deep crustal fluid released during metamorphism of subduction-accretion process. Bao et al. (2013) and Wang et al. (2017b) on the other hand propose that the LVZ in NW QO is an initial stage of the LVZ which has developed in the SGT and perhaps in the Southeast Tibetan Plateau since the evolution and growth of Tibetan Plateau began to the south and developed toward the north. In our model, NW QO is delineated by a weak mid-crustal LVZ between 15 and 35 km, as also supported by Li et al. (2014a), Li et al. (2017) and Wang et al. (2017b). Compared with the LVZ in SGT, the amplitude of LVZ in NW QO is weaker, whatever method we use to define the LVZ. This is in accordance with previous studies. The observed weaker low-velocity zones in NW QO possibly originate from aqueous fluids.

## 5. Conclusion

Deployment of dense network is now becoming common practice in seismology at different scales. Beamforming is well adapted to handle data from dense networks, including using ambient noise to study structural properties. A beamforming method is proposed in this study to extract the 2D phase velocities of Rayleigh waves from the noise field by dividing the network in appropriate subarrays and applying beamforming on overlapping subarrays. We analyse the trade-off between subarray dimensions and phase velocity precision for crustal studies and conclude that $2^o \times 2^o$ subarrays are appropriate for the ChinArray II network with average interstation distance at 30 km.

Compared to the traditional pure-path inversion method, beamforming offers a direct evaluation of the phase velocity. The velocity under the subarray only depends on the data from the stations located inside this subarray. Therefore, at periods relevant for crustal studies, the beamforming method can give a more robust velocity estimate than traditional pure-path inversion of teleseismic data, even though at the cost of a somewhat lower lateral resolution. The method can be used even if the noise is strongly dominated by one source of noise, as opposed to traditional noise interferometry which requires fairly well azimuthally distributed noise sources.

Rayleigh wave phase velocity maps at periods between 7 and 35 s are obtained in NE Tibet based on the Rayleigh wave dispersion curves of each subarray, and a 3D shear wave velocity model is built by depth inversion. Two mid-crustal LVZs beneath NW QO and SGT are observed between 15- and 35-km depth. The LVZ in SGT possibly extends northward of the East Kunlun Fault and may be related to mid-crustal partial melting. The observed weaker LVZs in NW QO possibly originate from aqueous fluids.

**Acknowledgments**
The dispersion curves and S-wave velocity model are openly available from the NIRD Research Data Archive (doi:10.11582/2020.00009). We thank Yonghua Li for providing the results of traditional surface wave tomography based on earthquake events. The discussion on the origin for the observed mid-crustal LVZ also benefited from talking with Yonghua Li. Xingchen Wang offered the data of Moho depth. This work was supported by the National Key R & D Program of China (2017YFC1500200), the National Natural Science Foundation of China (41674062, U1839209, 41174041), and the China National Special Fund for Earthquake Scientific Research of Public Interest (201308011). KW wishes to thank CEED, UiO, for hospitality during part of his work. VM acknowledges support from the Research Council of Norway through its centers of Excellence funding scheme, Project Number 223272. We thank Nicholas Harmon and two anonymous reviewers for their constructive comments that improved the manuscript greatly.

## References

Alsina, D., Snieder, R., & Maupin, V. (1993). A test of the great circle approximation in the analysis of surface waves. *Geophysical Research Letters*, *11*, 633–636.

Alvizuri, C., & Tanimoto, T. (2011). Azimuthal anisotropy from array analysis of Rayleigh waves in Southern California. *Geophysical Journal International*, *186*(3), 1135–1151.

Bao, X., Song, X., Xu, M., Wang, L., Sun, X., Mi, N., et al. (2013). Crust and upper mantle structure of the North China Craton and the NE Tibetan Plateau and its tectonic implications. *Earth and Planetary Science Letters*, *369*, 129–137.

Bao, X., Sun, X., Xu, M., Eaton, D., Song, X., Wang, L., et al. (2015). Two crustal low-velocity channels beneath SE Tibet revealed by joint inversion of Rayleigh wave dispersion and receiver functions. *Earth and Planetary Science Letters*, *415*, 16–24.

Behr, Y., Townend, J., Bowen, M., Carter, L., Gorman, R., Brooks, L., & Bannister, S. (2013). Source directionality of ambient seismic noise inferred from three-component beamforming. *Journal of Geophysical Research: Solid Earth*, *118*, 240–248. https://doi.org/10.1029/2012JB009382

Bendick, R., & Flesch, L. (2007). Reconciling lithospheric deformation and lower crustal flow beneath central Tibet. *Geology*, *35*(10), 895–898.

Bensen, G., Ritzwoller, M., Barmin, M., Levshin, A., Lin, F., Moschetti, M., et al. (2007). Processing seismic ambient noise data to obtain reliable broad-band surface wave dispersion measurements. *Geophysical Journal International*, *169*(3), 1239–1260.

Bodin, T., & Maupin, V. (2008). Resolution potential of surface wave phase velocity measurements at small arrays. *Geophysical Journal International*, *172*, 698–706. https://doi.org/10.1111/j.1365-246X.2007.03668.x

Campillo, M., Sato, H., Shapiro, N. M., & van der Hilst, R. D. (2011). New developments on imaging and monitoring with seismic noise Foreword. *Comptes Rendus Geoscience*, *343*(8-9), 487–495. https://doi.org/10.1016/j.crte.2011.07.007

Clark, M. K., & Royden, L. H. (2000). Topographic ooze: Building the eastern margin of Tibet by lower crustal flow. *Geology*, *28*(8), 703–706.

England, P., & Houseman, G. (1986). Finite strain calculations of continental deformation: 2. Comparison with the India-Asia collision zone. *Journal of Geophysical Research*, *91*(B3), 3664–3676.

Forsyth, D. W., & Li, A. (2005). Array analysis of two-dimensional variations in surface wave phase velocity and azimuthal anisotropy in the presence of multipathing interference. *In Seismic Earth: Array Analysis of Broadband Seismograms, Geophys Monogr. Ser.*, *187*, 81–97.

Friederich, W. (1998). Wave-theoretical inversion of teleseismic surface waves in a regional network: Phase-velocity maps and a three-dimensional upper-mantle shear-wave-velocity model for southern Germany. *Geophysical Journal International*, *132*, 203–225. https://doi.org/10.1046/j.1365-246x.1998.00425.x

Friederich, W., Hunzinger, S., & Wielandt, E. (1998). A note on the interpretation of seismic surface waves over three-dimensional structures. *Geophysical Journal International*, *143*, 335–339. https://doi.org/10.1046/j.1365-246X.2000.01241.x.

Froment, B., Campillo, M., Roux, P., Goudard, P., Verdel, A., & Weaver, R. L. (2010). Estimation of the effect of nonisotropically distributed energy on the apparent arrival time in correlations. *Geophysics*, *75*(5), SA85CSA93. https://doi.org/10.1190/1.3483102

Gerstoft, P., & Tanimoto, T. (2007). A year of microseisms in Southern California. *Geophysical Research Letters*, *34*, L20304. https://doi.org/10.1029/2007GL031091

Harmon, N., Gerstoft, P., Rychert, C. A., Abers, G. A., de La Cruz, M. S., & Fischer, K. M. (2008). Phase velocities from seismic noise using beamforming and cross correlation in Costa Rica and Nicaragua. *Geophysical Research Letters*, *35*, L19303. https://doi.org/10.1029/2008GL035387

Jiang, C., Yang, Y., & Zheng, Y. (2014). Penetration of mid-crustal low velocity zone across the Kunlun fault in the ne Tibetan Plateau revealed by ambient noise tomography. *Earth and Planetary Science Letters*, *406*, 81–92. https://doi.org/10.1016/j.epsl.2014.08.040

Kennett, B., Engdahl, E., & Buland, R. (1995). Constraints on seismic velocities in the earth from travel times. *Geophysical Journal International*, *122*, 108–124.

Laske, G., Masters, G., Ma, Z., & Pasyanos, M. (2013). Update on CRUST1.0 - A 1-degree Global Model of Earth's Crust.

Lévêque, J., Cara, M., & Rouland, D. (1991). Waveform inversion of surface wave data: Test of a new tool for systematic investigation of upper mantle structures. *Geophysical Journal International*, *104*(3), 565–581.

Li, Y., Pan, J., Wu, Q., & Ding, Z. (2017). Lithospheric structure beneath the northeastern Tibetan Plateau and the western Sino-Korea Craton revealed by Rayleigh wave tomography. *Geophysical Journal International*, *210*(2), 570–584.

Li, H., Shen, Y., Huang, Z., Li, X., Gong, M., Shi, D., et al. (2014a). The distribution of the mid-to-lower crustal low-velocity zone beneath the northeastern Tibetan Plateau revealed from ambient noise tomography. *Journal of Geophysical Research: Solid Earth*, *119*(3), 1954–1970.

Lin, F. C., Ritzwoller, M. H., & Snieder, R. (2009). Eikonal tomography: Surface wave tomography by phase front tracking across a regional broad-band seismic array. *Geophysical Journal International*, *177*(3), 1091–1110. https://doi.org/10.1111/j.1365-246X.2009.04105.x

Liu, Q., Hilst, R. D. V. D., Li, Y., Yao, H. J., Chen, J. H., Guo, B., et al. (2014). Eastward expansion of the Tibetan Plateau by crustal flow and strain partitioning across faults. *Nature Geoscience*, *7*(5), 361–365. https://doi.org/10.1038/ngeo2130

Liu, M. J., Mooney, W. D., Li, S., Okaya, N., & Detweiler, S. (2006). Crustal structure of the northeastern margin of the Tibetan plateau from the Songpan-Ganzi terrane to the Ordos basin. *Tectonophysics*, *420*(1-2), 253–266. https://doi.org/10.1016/j.tecto.2006.01.025

Lu, L., Wang, K., & Ding, Z. (2018). The effect of uneven noise source and/or station distribution on the estimation of azimuth anisotropy of surface waves. *Earthquake Science*, *31*(4), 175–186. https://doi.org/10.29382/eqs-2018-0175-1

Maupin, V. (2011). Upper-mantle structure in southern Norway from beamforming of Rayleigh wave data presenting multipathing. *Geophysical Journal International*, *185*(2), 985–1002. https://doi.org/10.1111/j.1365-246x.2011.04989.x

Maupin, V., & Cara, M. (1992). Love-Rayleigh wave incompatibility and possible deep upper mantle anisotropy in the Iberian Peninsula. *Pure and Applied Geophysics*, *138*(3), 429–444. https://doi.org/10.1007/bf00876881

Molnar, P., & Tapponnier, P. (1975). Cenozoic tectonics of asia: Effects of a continental collision. *Science*, *189*(4201), 419–426. https://doi.org/10.1126/science.189.4201.419

Montagner, J. (1986). Regonal three-dimensional structures using long-period surface waves. *Annales Geophysicae*, *4*, 283–294.

Pan, J., Li, Y., Wu, Q., Ding, Z., & Yu, D. (2017). Phase velocity maps of Rayleigh wave based on a dense coverage and portable seismic array in NE Tibetan Plateau and its adjacent regions. *Chinese Journal of Geophysics*, *60*(6), 2291–2303. https://doi.org/10.6038/cjg20170621

Ritzwoller, M. H., Lin, F. C., & Shen, W. (2011). Ambient noise tomography with a large seismic array. *Comptes Rendus Geoscience*, *343*(8-9), 558–570. https://doi.org/10.1016/j.crte.2011.03.007

Romanowicz, B. (2002). Inversion of surface waves: A review. *International Handbook of Earthquake and Engineering Seismology*, *81A*, 149–173.

Rost, S., & Thomas, C. (2002). Array seismology: Methods and applications. *Reviews of Geophysics*, *40*(3), 2–1–2-27. https://doi.org/10.1029/2000RG000100

Roux, P., & Ben-Zion, Y. (2017). Rayleigh phase velocities in Southern California from beamforming short-duration ambient noise. *Geophysical Journal International*, *211*(1), 450–454. https://doi.org/10.1093/gji/ggx316

Royden, L. H., Burchfiel, B. C., & van der Hilst, R. D. (2008). The geological evolution of the Tibetan Plateau. *Science*, *321*(5892), 1054–1058. https://doi.org/10.1126/science.1155371

Ruigrok, E., Gibbons, S., & Wapenaar, K. (2017). Cross-correlation beamforming. *Journal of Seismology*, *21*(3), 495–508. https://doi.org/10.1007/s10950-016-9612-6

Sadeghisorkhani, H., Gudmundsson, O., Roberts, R., & Tryggvason, A. (2017). Velocity-measurement bias of the ambient noise method due to source directivity: A case study for the Swedish National Seismic Network. *Geophysical Journal International*, *209*(3), 1648–1659. https://doi.org/10.1093/gji/ggx115

Sens-Schöenfelder, C., & Wegler, U. (2011). Passive image interferometry for monitoring crustal changes with ambient seismic noise. *Comptes Rendus Geoscience*, *343*(8-9), 639–651. https://doi.org/10.1016/j.crte.2011.02.005

Shapiro, N. M., Campillo, M., Stehly, L., & Ritzwoller, M. H. (2005). High-Resolution surface-wave tomography from ambient seismic noise. *Science*, *307*(5715), 1615–1618. https://doi.org/10.1126/science.1108339

Tapponnier, P., & Molnar, P. (1997). Active faulting and tectonics in China. *Journal of Geophysical Research*, *82*(20), 2905–2930. https://doi.org/10.1029/jb082i020p02905

Tarantola, A., & Valette, B. (1982). Generalized nonlinear inverse problems solved using the least squares criterion. *Reviews of Geophysics*, *20*(2), 219–232. https://doi.org/10.1029/RG020i002p00219

Tomar, G., Shapiro, N. M., Mordret, A., Singh, S. C., & Montagner, J. P. (2017). Radial anisotropy in Valhall: Ambient noise-based studies of Scholte and Love waves. *Geophysical Journal International*, *208*(3), 1524–1539. https://doi.org/10.1093/gji/ggw480

Tsai, V. C. (2009). On establishing the accuracy of noise tomography travel-time measurements in a realistic medium. *Geophysical Journal International*, *178*, 1555–1564. https://doi.org/10.1111/j.1365-246X.2009.04239.x

Wang, X., Ding, Z., Wu, Y., & Zhu, L. (2017a). Crustal thicknesses and Poisson's ratios beneath the northern section of the north-south seismic belt and surrounding areas in China. *Chinese Journal of Geophysics*, *60*(6), 2080–2090. https://doi.org/10.6038/cjg20170605

Wang, X., Li, Y., Ding, Z., Zhu, L., Wang, C., Bao, X., & Wu, Y. (2017b). Three-dimensional lithospheric S wave velocity model of the NE Tibetan Plateau and western North China craton. *Journal of Geophysical Research: Solid Earth*, *122*, 6703–6720. https://doi.org/10.1002/2017JB014203

Wathelet, M., Jongmans, D., Ohrnberger, M., & Bonnefoy-Claudet, S. (2008). Array performances for ambient vibrations on a shallow structure and consequences over $V_S$ inversion. *Journal of Seismology*, *12*(1), 1–19. https://doi.org/10.1007/s10950-007-9067-x

Weidle, C. (2012). Surface wave phase velocity maps from multiscale wave field interpolation. *Computational Geosciences*, *16*(3), 535–549. https://doi.org/10.1007/s10596-011-9269-8

Wielandt, E. (1993). Propagation and structural interpretation of non-plane waves. *Geophysical Journal International*, *113*(1), 45–53. https://doi.org/10.1111/j.1365-246X.1993.tb02527.x

Woodhouse, J., & Dziewonski, A. (1984). Mapping the upper mantal: Three dimensional modeling of the Earth structure by inversion of seismic waveforms. *Journal of Geophysical Research*, *89*, 5953–5986.

Yang, Y., Ritzwoller, M. H., Zheng, Y., Shen, W., Levshin, A. L., & Xie, Z. (2012). A synoptic view of the distribution and connectivity of the mid-crustal low velocity zone beneath Tibet. *Journal of Geophysical Research*, *117*, B04303. https://doi.org/10.1029/2011JB008810

Yang, Y., Zheng, Y., Chen, J., Zhou, S., Celyan, S., Sandvol, E., et al. (2010). Rayleigh wave phase velocity maps of Tibet and the surrounding regions from ambient seismic noise tomography. *Geochemistry, Geophysics, Geosystems*, *11*, Q08010. https://doi.org/10.1029/2010GC003119

Yao, H., & van der Hilst, R. (2009). Analysis of ambient noise energy distribution and phase velocity bias in ambient noise tomography, with application to SE Tibet. *Geophysical Journal International*, *179*(2), 1113–1132. https://doi.org/10.1111/j.1365-246X.2009.04329.x

Zhan, Y., Zhao, G., Wang, L., Wang, J., Chen, X., Zhao, L., & Xiao, Q. (2014). Deep electric structure beneath the intersection area of west Qinling orogenic zone with north-south seismic tectonic zone in China. *Chinese Journal of Geophysics*, *57*(8), 2594–2607. https://doi.org/10.6038/cjg20140819

Zhao, L., Zhan, Y., Chen, X., Yang, H., & Jiang, F. (2015). Deep electrical structure of the central west Qinling orogenic belt and blocks on its either side. *Chinese Journal of Geophysics*, *58*(7), 2460–2472. https://doi.org/10.6038/cjg20150722

Zhong, S., Wu, J., Fang, L., Wang, W., Fan, L., & Wang, H. (2017). Surface wave eikonal tomography in and around the northeastern margin of the Tibetan Plateau. *Chinese Journal of Geophysics*, *60*, 2304–2314. https://doi.org/10.6038/cjg20170622